The Astrophysical Journal, 570:637–646, 2002 May 10

THE INFLUENCE OF ELECTRON TEMPERATURE AND MAGNETIC FIELD STRENGTH ON COSMIC-RAY INJECTION IN HIGH MACH NUMBER SHOCKS

H. Schmitz and S. C. Chapman
Space and Astrophysics Group, Department of Physics, University of Warwick, Coventry CV4 7AL, UK; holgers@astro.warwick.ac.uk
and
R. O. Dendy
UKAEA Fusion, Culham Science Centre, Abingdon, Oxfordshire OX14 3DB, UK
Received 2001 August 29; accepted 2002 January 22

ABSTRACT

Electron preacceleration from thermal to mildly relativistic energies in high Mach number shocks (the injection problem) is an outstanding issue in understanding synchrotron radiation from supernova remnants. At high Alfvénic Mach numbers, collisionless perpendicular shocks reflect a fraction of the upstream ions. This gives rise to two-stream instabilities, which in turn can accelerate ions. However, in astrophysical plasmas, the value of β—the ratio of kinetic pressure to magnetic pressure—is not well known. We have used a particle in cell simulation code to investigate the influence of β on the shock structure and on the electron acceleration (assuming thermodynamic equilibrium in the undisturbed plasma, $\beta = \beta_i = \beta_e$). Previous simulations at low values of β showed that the phase space distributions of electrons and ions became highly structured: characteristic holes appear in the electron phase space, and the shock dynamics exhibit reformation processes. However, we find that all these features disappear at higher β due to the high initial thermal velocity of the electrons. It follows that the electron cosmic-ray injection mechanism depends strongly on β, that is, on the electron temperature normalized to the magnetic field upstream.

Subject headings: acceleration of particles — shock waves — supernovae: general

1. INTRODUCTION

Observations of shell-type supernova remnants (SNRs) show that these objects emit synchrotron radiation, which indicates the presence of energetic electrons, typically in the range of GeV. Some SNRs emit even up to X-ray wavelengths (Pohl & Esposito 1998) corresponding to electron energies of up to 10^{14} eV. Higher resolution measurements (Koyama, Petre, & Gotthelf 1995) show that the highest energy emission originates from the rim, and its spectrum is hard, almost power law. The region of this emission has sharp, clearly defined edges, whereas the emission from the center has a softer spectrum with large atomic line components. This leads to the conclusion that electrons are accelerated in the shock upstream of the SNR ejecta in the interstellar medium.

Several mechanisms are known to accelerate particles in collisionless shocks. In shock drift acceleration, the gradient in the magnetic field causes electrons to drift parallel to the shock front, where they are accelerated by the electric field $\boldsymbol{u}_{\rm shock} \times \boldsymbol{B}_1$ arising from the motion of the shock with velocity $\boldsymbol{u}_{\rm shock}$ through an undisturbed plasma with magnetic field $\boldsymbol{B}_1$ in the shock frame of reference. The electrons thus form a high-velocity electron beam. This mechanism is not present in parallel shocks since they do not have a motional electric field, $\boldsymbol{u}_{\rm shock} \times \boldsymbol{B}_1 = 0$. Giacalone et al. (1993) have found that parallel shocks can, in some cases, exhibit features of perpendicular shocks. This is because strong fluctuations in the transverse component of the magnetic field can cause the local field to be directed almost perpendicular to the shock normal. However, drift acceleration was not dominant in these cases. In perpendicular shocks, on the other hand, drift acceleration is limited because the electrons encounter the shock only for a finite time. Thus, unless there is a mechanism for the electrons to encounter the shock front repeatedly, there is an upper limit on the energy.

First-order Fermi acceleration results from particles repeatedly crossing the shock. The upstream and downstream flows carry coherent structures (generated by turbulence) that are embedded in the flows and thus are moving on the average with the flow velocities. Bell (1978) showed that even the normally undisturbed upstream region will always exhibit fluctuations that are induced by the accelerated electrons themselves. In the shock frame, the upstream velocity is much higher than the downstream velocity, and so the two regions can be regarded as two converging flows. An electron repeatedly crossing the shock front by scattering off the comoving turbulence structures and thus repeatedly encountering the two converging flows will be accelerated. In perpendicular shocks, however, the particles at background temperature cannot move freely along the shock normal because of the magnetic field. For this reason, only parallel shocks can directly accelerate particles from the background population by means of the first-order Fermi mechanism. However, if particles have been preaccelerated, the Larmor radius can become large compared to the mean free path for scattering on coherent structures so that Fermi acceleration is then possible (Jokipii 1987).

In second-order Fermi acceleration, particles do not have to cross the shock front. They scatter off magnetic fluctuations on the same (downstream) side of the shock. Apart from the average flow velocity, these fluctuations have a random velocity component. A particle scattering on these fluctuations can be accelerated in a head-on collision or decelerated in a retreating collision. In first-order, a particle therefore is not accelerated. A second-order effect is that, on the average, there are more head-on collisions than retreating ones, and due to this, the particles are accelerated. This

mechanism works at both parallel and perpendicular shocks; however, it is much less efficient than first-order Fermi acceleration. First- and second-order Fermi acceleration are often referred to as diffusive shock acceleration (Giacalone et al. 1993).

It follows that diffusive shock acceleration can only efficiently accelerate electrons that already have a high energy compared to the background thermal energy, which means they have to be mildly relativistic. The nature of the preacceleration mechanism (the injection problem) still remains an open question (Levinson 1997). For the case of perpendicular shocks, Papadopoulos (1988) proposed that instabilities caused by the ions reflected off the shock and returning to it (thus creating the foot of the shock) could produce the necessary electron acceleration. The resulting ion beams are Buneman unstable if their relative velocity $u_{\rm rel}$ is greater than the thermal velocity $v_{e,\rm th}$ of the electrons (Buneman 1958). Assuming that $u_{\rm rel} = 2u_1$, where u_1 is the upstream, or equivalently, the shock velocity, this condition can be written

$$2\frac{M_{\rm A}}{\beta}\frac{m}{M} > 1 \ . \tag{1}$$

Here $M_{\rm A}$ is the Alfvénic Mach number of the shock, β is the local ratio of kinetic to magnetic pressure, and m and M are the electron and ion rest masses. Waves generated by the Buneman instability can heat electrons rapidly on the timescale of the electron plasma frequency and could contribute to the preacceleration of the electrons (Papadopoulos 1988). A number of hybrid simulations have been carried out to investigate this question (see, e.g., Cargill & Papadopoulos 1988; Giacalone et al. 1993; Burgess, Wilkinson, & Schwartz 1989); however, these typically assume a thermal electron distribution and cannot account for nonthermal electron heating or acceleration. Recently, Shimada & Hoshino (2000) have taken the subject further by simulating a high Mach number perpendicular shock with a fully kinetic particle in cell code. In their simulations, the ratio of kinetic to magnetic pressure $\beta = \beta_i = \beta_e$ was fixed at a single value. However, the value of β in SNR shocks is uncertain, and one can expect different physical processes to arise for different values of β. It is therefore our aim in this paper to repeat the (computationally intensive) simulations of Shimada & Hoshino for two different values of β and to compare the shock behavior and the electron acceleration in the two cases.

2. SIMULATION

We use a relativistic electromagnetic particle in cell (PIC) code to simulate the structure and development of a high Alfvénic Mach number (of the order of 10) magnetosonic shock. In PIC simulations, the distribution functions of ions and electrons are represented by computational particles, while the electromagnetic field is given on a grid in configuration space. The particles and the fields are advanced in time by means of a leapfrog algorithm which uses the Lorentz force to accelerate and move the superparticles and Maxwell's equations to advance the fields. Details of the PIC simulation technique are described by Hockney & Eastwood (1981). The PIC approach enables self-consistent simulations of plasmas that are far from equilibrium, where arbitrary distribution functions can develop.

The code that we use to simulate the shock is described by Devine (1995) and has been used recently to investigate electron acceleration in the foot of SNR shocks (Dieckmann et al. 2000). This code is relativistic and can therefore be used to simulate high-energy processes. Relativistic electromagnetic PIC codes have been used previously to simulate acceleration processes in astrophysical plasmas (see, e.g., McClements et al. 1993; Bessho & Ohsawa 1999). The code is a $1x3v$ code, meaning that all (vector) field and bulk plasma quantities are a function of one-configuration space coordinate (x) and time, while all three velocity components (or equivalently all three components of the momenta p) of each particle are followed. Physically this means the simulated shock is assumed to be homogeneous in those directions. Importantly, in this $1x3v$ configuration, $\nabla \cdot \boldsymbol{B} = 0$, so $B_x = \text{const} = 0$. Reduced dimensionality places constraints on particle motion that can prohibit cross-field transport. Specifically, the particles can be shown to be confined to a given flux tube provided their energy is constant (Northrup & Teller 1960; Cowley 1977; Giacalone & Jokipii 1994; Jones, Jokipii, & Baring 1998; Jokipii 1993; Chapman & Cowley 1984).

In common with Shimada & Hoshino (2000), we use the piston method (Burgess et al. 1989 and references therein) to set up the shock: we inject particles (electrons and ions) on the left side of the simulation box, while the right boundary is taken to be completely reflecting of both particles and waves. This is the equivalent of a perfectly reflecting and perfectly conducting wall. The injected particles have a high x-directed velocity component $u_{\rm flow}$, which we will refer to as the upstream inflow velocity, and a random thermal velocity, which corresponds to the upstream temperature T_1 (the indices 1 and 2 refer to the upstream and the downstream values, respectively). The magnetic field at the upstream (left) boundary is fixed at $B_{z,1}$. The reflecting boundary condition on the right eventually creates a stationary plasma in the rightmost area of the simulation box. A shock then forms at the right boundary and propagates to the left. While it has been shown in hybrid simulations that quasi-parallel shocks depend strongly on the mechanisms by which they are created (Cargill 1991), quasi- and purely perpendicular shocks do not depend on the initiation mechanism (Giacalone et al. 1993).

After some time—depending on the size of the simulation box—the shock will have traveled through the system and reached the left boundary. In order to simulate the shock for longer times without increasing the size of the simulation box, we have developed a simple shock-following algorithm which is described in the Appendix. More complicated algorithms are possible (see, e.g., Bennett & Ellison 1995), where the goal is to simulate Fermi acceleration in a parallel shock with clearly defined free escape boundaries and self-consistent downstream boundary conditions. In the present problem, however, it will be seen that flux of energetic particles reaching the upstream boundary is negligible, so that we do not require free escape boundaries. Furthermore, there are no high-energy particles entering the simulation box from the downstream region that might affect the downstream boundary conditions.

The dimension of a grid cell is set equal to the initial Debye length for numerical stability reasons (Hockney & Eastwood 1981), while the size of the simulation box is set to about 30 times the upstream ion Larmor radius $\lambda_{ci,1}$ cal-

TABLE 1
NORMALIZATIONS USED IN THIS PAPER

Quantity	Normalized by
Velocities u	Flow velocity of the upstream plasma $u_{\rm flow}$
Magnetic field B	Upstream magnetic field $B_{z,1}$
Electric field	$u_{\rm flow} B_{z,1}$
x-coordinate	Ion Larmor radius λ_{ci}

culated with the upstream velocity u_1. Initially, each grid cell contains about 100 particles of each species. In the following, we will normalize the quantities as given in Table 1.

3. RESULTS

Here we show the results of two simulations with different plasma β, where

$$\beta = \frac{nkT_1}{B_{z,1}^2/2\mu_0}\,, \tag{2}$$

and thermodynamic equilibrium in the undisturbed plasma is assumed, $T_{i,1} = T_{e,1} \equiv T_1$. The first simulation with $\beta = 0.15$ corresponds to the shock simulated by Shimada & Hoshino (2000), while the second simulation has a considerably higher value of $\beta = 1$. The other parameters in both simulations are chosen to be the same as in the Shimada & Hoshino case: the ratio of electron plasma to Larmor frequency $\omega_{pe}/\Omega_{ce} = 20$ and the ratio of ion to electron mass $M/m = 20$. The Alfvénic Mach number of $M_{\rm A} = 10.5$ corresponds to the high Mach number run of Shimada & Hoshino. The upstream perpendicular magnetic field (not specified by Shimada & Hoshino) is assumed here to be $B_{z,1} = 10^{-7}$ T. This value is consistent with those expected in supernova remnants (Ellison & Reynolds 1991). With this choice of parameters, the upstream temperature is 95.9 eV for the $\beta = 0.15$ case and 639 eV for the $\beta = 1$ case.

The first simulation with $\beta = 0.15$ corresponds to that value investigated by Shimada & Hoshino (2000). Figure 1 shows the ion and electron p_x versus x phase space distributions at $t \approx 2.5/\omega_{ci}$. Here $\omega_{ci} = eB_{z,1}/M$ is the upstream ion cyclotron frequency. Also shown is the perpendicular magnetic field B_z and the parallel electric field E_x. The particle inflow is from the left, while the reflecting boundary is located to the left, outside of the plot at $x \approx 25\ \lambda_{ci}$. The simulation with $\beta = 0.15$ indeed reconstructs the results of Shimada & Hoshino (2000). The shock shows a complex structure, with a high fraction of the ions reflected at the shock, forming the upstream foot of the shock starting at $x \approx 1.5\ \lambda_{ci}$. The electrons are decelerated over a short distance when they enter the foot region. Also, it can be seen that the parallel electric field shows the strongest fluctuations inside the small foot region. The magnetic overshoot is located at $x \approx 3.5\ \lambda_{ci}$. This position is referred to as the shock position. At the point in time the figure refers to, the shock is well separated from the right wall. (Note that the origin of Fig. 1 does not coincide with the origin of the simulation box but is chosen to be consistent throughout this paper. Also the time $t = 0$ does not refer to the start of the simulation but to the origin in Figs. 4 and 5, respectively. At the time $t = 0$, the simulation has run for $\approx 19.5/\omega_{ci}$ and can be assumed to be in a state independent from the initial conditions.)

Figure 2 shows details of the foot region. One can observe that the reflected ion beam interacts with the incoming ions causing a two-stream instability. At the leftmost part of the foot, small disturbances of the ion beam directed down-

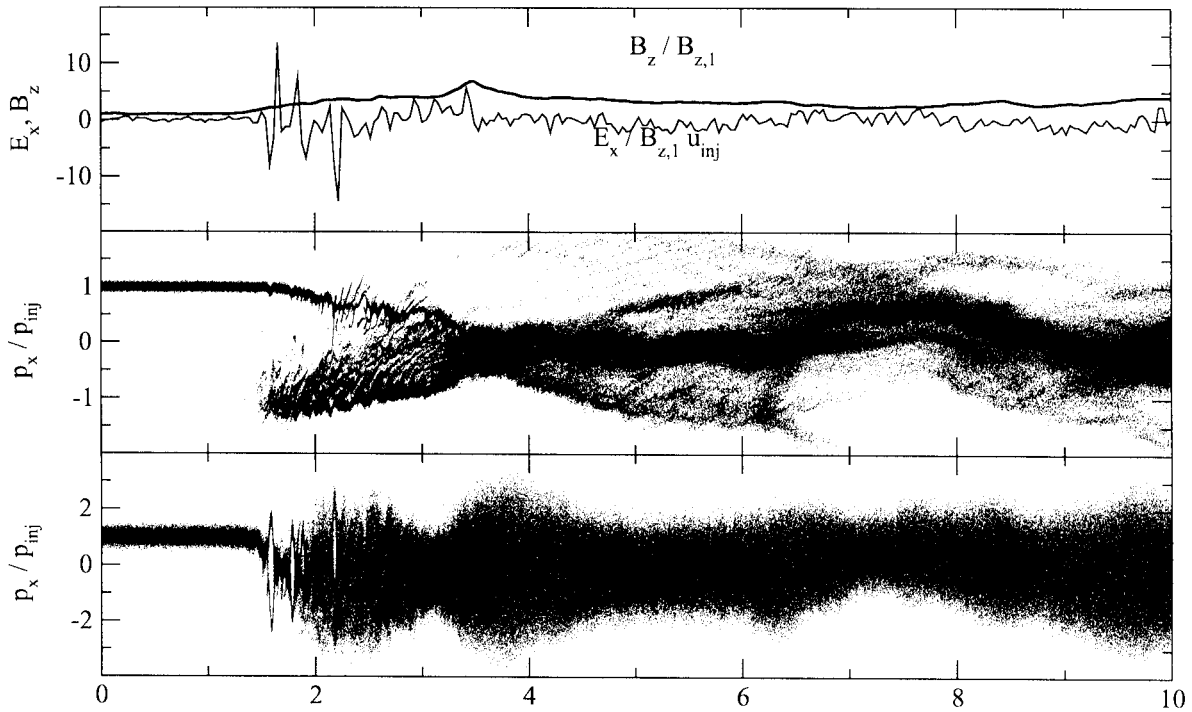

FIG. 1.—Parallel electric and perpendicular magnetic field (*upper panel*), ion phase space distribution (*middle panel*), and electron phase space distribution (*lower panel*) at $t\omega_{ci} \approx 2.5$ for $\beta = 0.15$. Particle inflow is from the left; the right boundary is situated far right of this plot at $x/\lambda_c i \approx 25$. The frame of reference is the downstream rest frame.

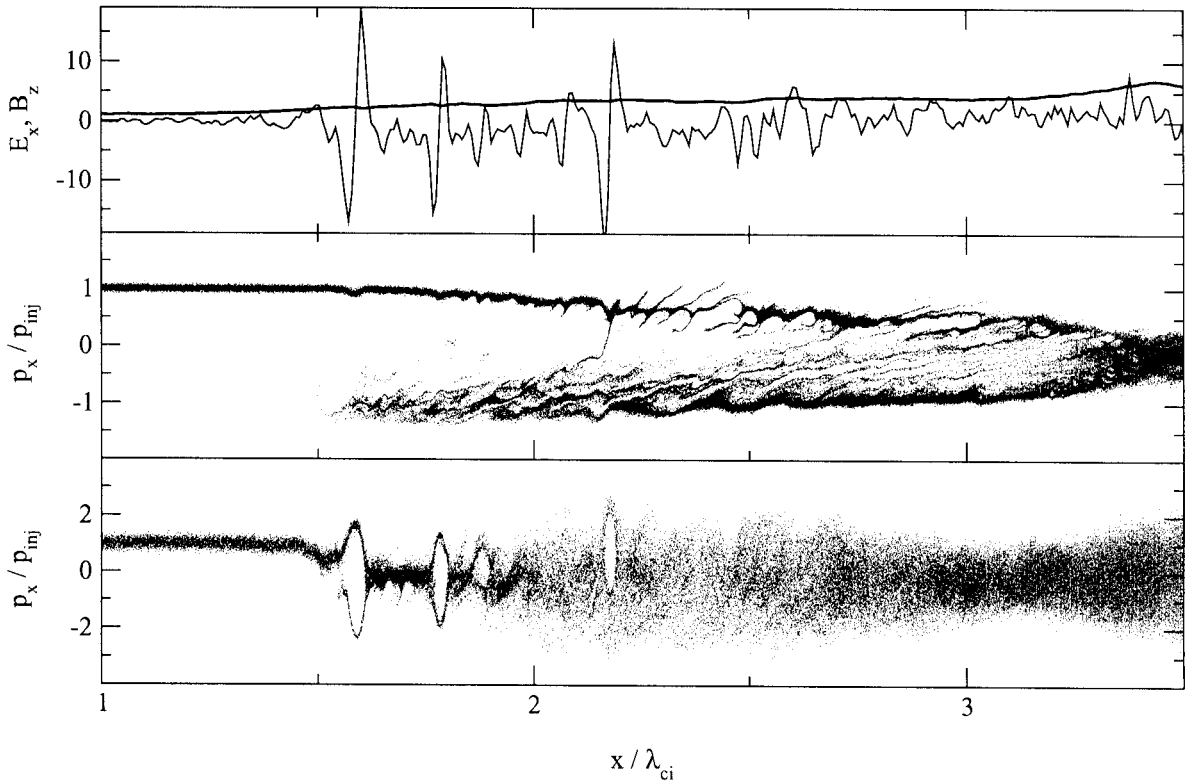

FIG. 2.—Detail of Fig. 1 showing only the foot region of the shock

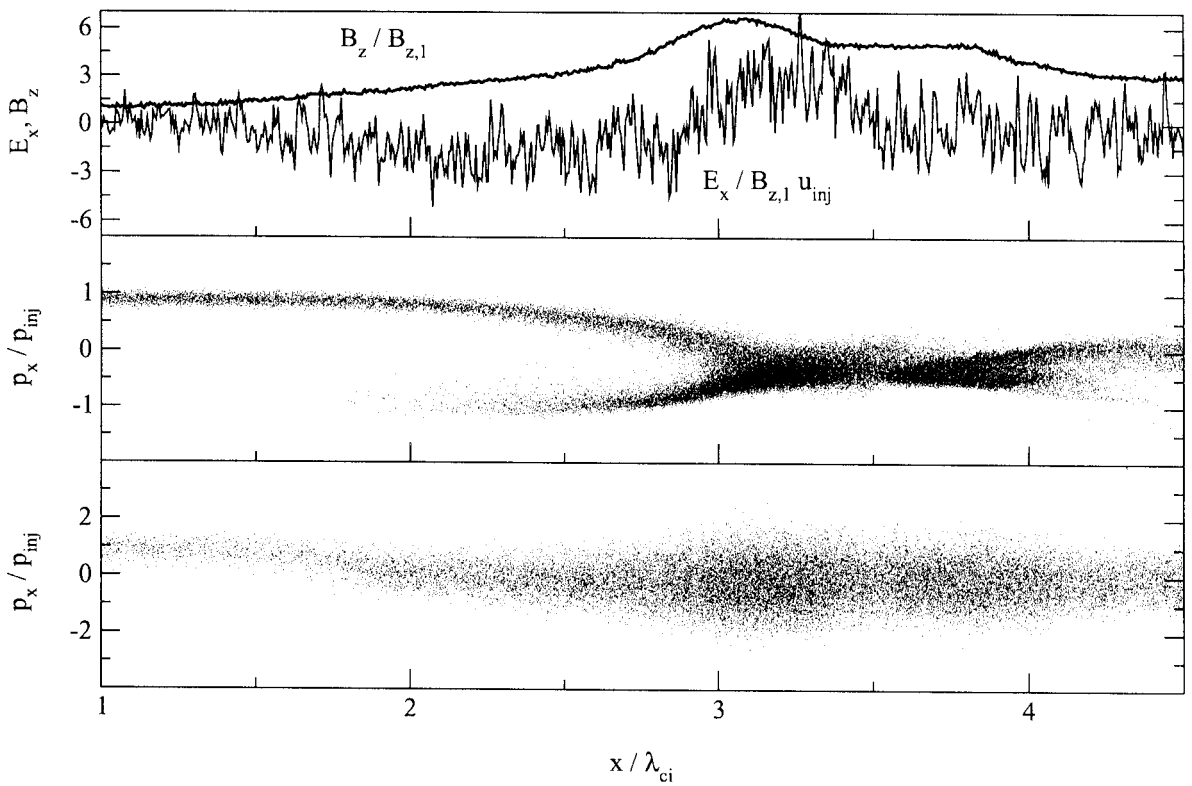

FIG. 3.—Parallel electric and perpendicular magnetic field (*upper panel*), ion phase space distribution (*middle panel*), and electron phase space distribution (*lower panel*) in the foot of the shock at $t\omega_{ci} \approx 3$ for $\beta = 1$ in the downstream rest frame.

stream can be seen; these correspond to fluctuations of the local upstream-directed ion beam. The disturbances gradually become larger toward the right of the foot, where the beam shows complex structure, and the largest disturbances are associated with peaks in the electric field. Turning to the electron phase space distribution, we see that the positions of these peaks of the electric field coincide with holes in electron phase space, but otherwise, the electron phase space distribution shows little structure. The electrons are decelerated almost instantly when they enter the foot, while their directed kinetic energy is converted into random motion.

In contrast, the simulations with $\beta = 1$ show no small-scale structure (see Fig. 3). This figure again focuses on the foot region of the shock. As in the low-β case, a fraction of the ions is reflected at the shock front and forms the foot of the shock. While the ion phase space distribution in the region downstream of the shock still shows structure, there is now no small-scale structure in the foot region. The incoming ions and electrons have a higher thermal speed compared to the upstream flow velocity than in the $\beta = 0.15$ case. This means that the growth rate for the Buneman instability is slower (Buneman 1958). The ions do not stay in the foot long enough to drive waves so that they would be visible in the ion phase space distribution. The deceleration of the electrons is more smooth and takes place throughout the entire foot; their distribution in phase space appears to be thermal apart from a superimposed, directed momentum. Also, no large peaks in the electric field are present, and the fluctuations of E_x on small length scales have lower amplitude than those on large length scales.

We now consider the temporal behavior of the shock. Figure 4 shows the perpendicular magnetic field as a function of position and time for the $\beta = 0.15$ case and displays the nonstationary behavior of the shock front. The magnetic overshoot region, corresponding to the maximum in the magnetic field, moves back and forth in the shock in a more or less periodic fashion on the timescale of the ion cyclotron period. The magnetic overshoot is repeatedly pushed back into the downstream region, while a new maximum in B_z is created further upstream. At the same time, the size of the foot of the shock increases and decreases. This periodic fluctuation of the fraction of reflected ions has been reported by Quest (1986). In the foot formation period starting at about $t\omega_{ci} = 2$, one can clearly see that, while the size of the foot is increasing, a wave with phase velocity directed upstream travels into the foot. These waves have a wavelength of order the electron Larmor radius. As the shock progresses through a cycle, the phase velocity of these waves decreases and reaches zero before increasing again. The region where these waves are visible moves into the downstream region together with the magnetic field maximum. Shortly before the maximum extension of the foot,

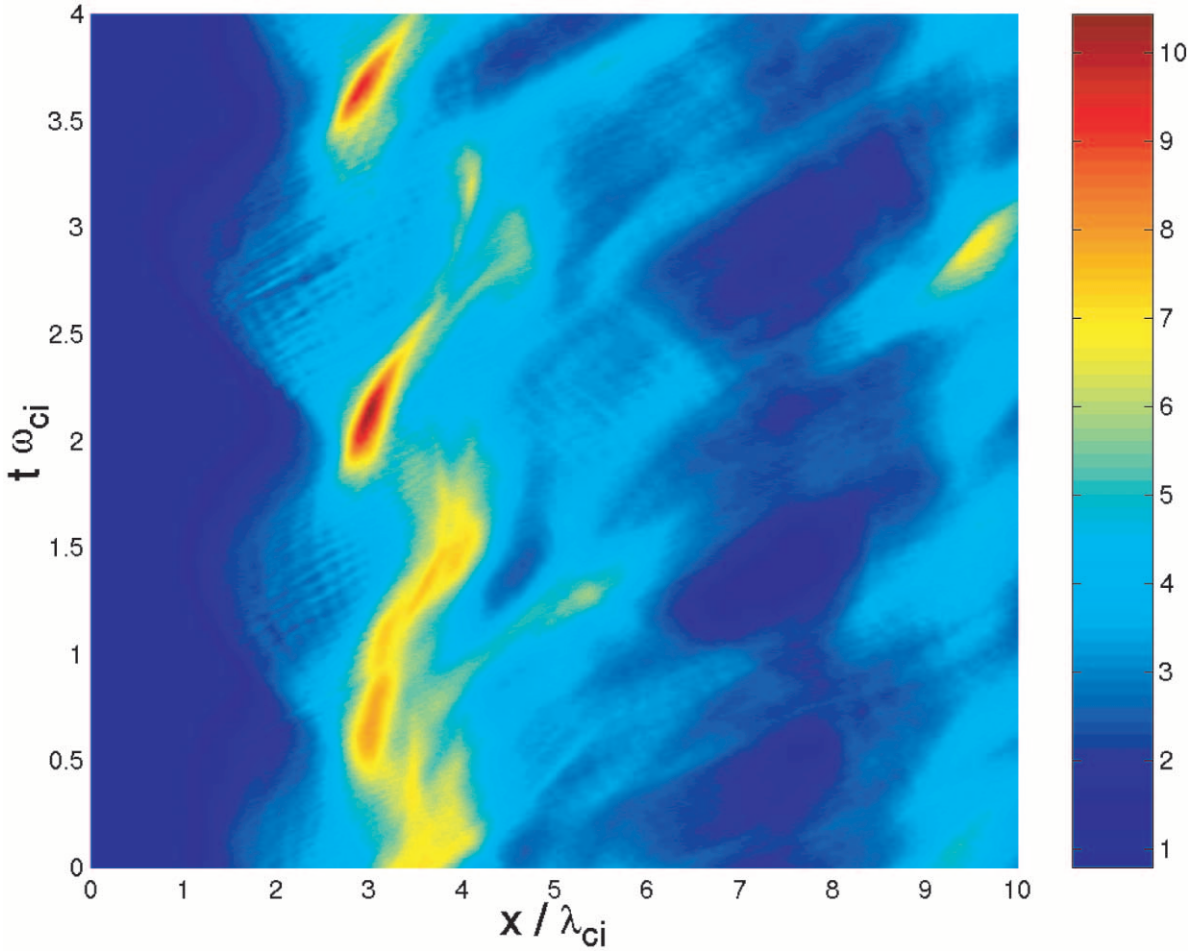

FIG. 4.—Perpendicular magnetic field component B_z as a function of position and time for $\beta = 0.15$. The field is normalized to the upstream magnetic field. The frame of reference has been changed to the shock rest frame to emphasize the time dependent behavior of the shock.

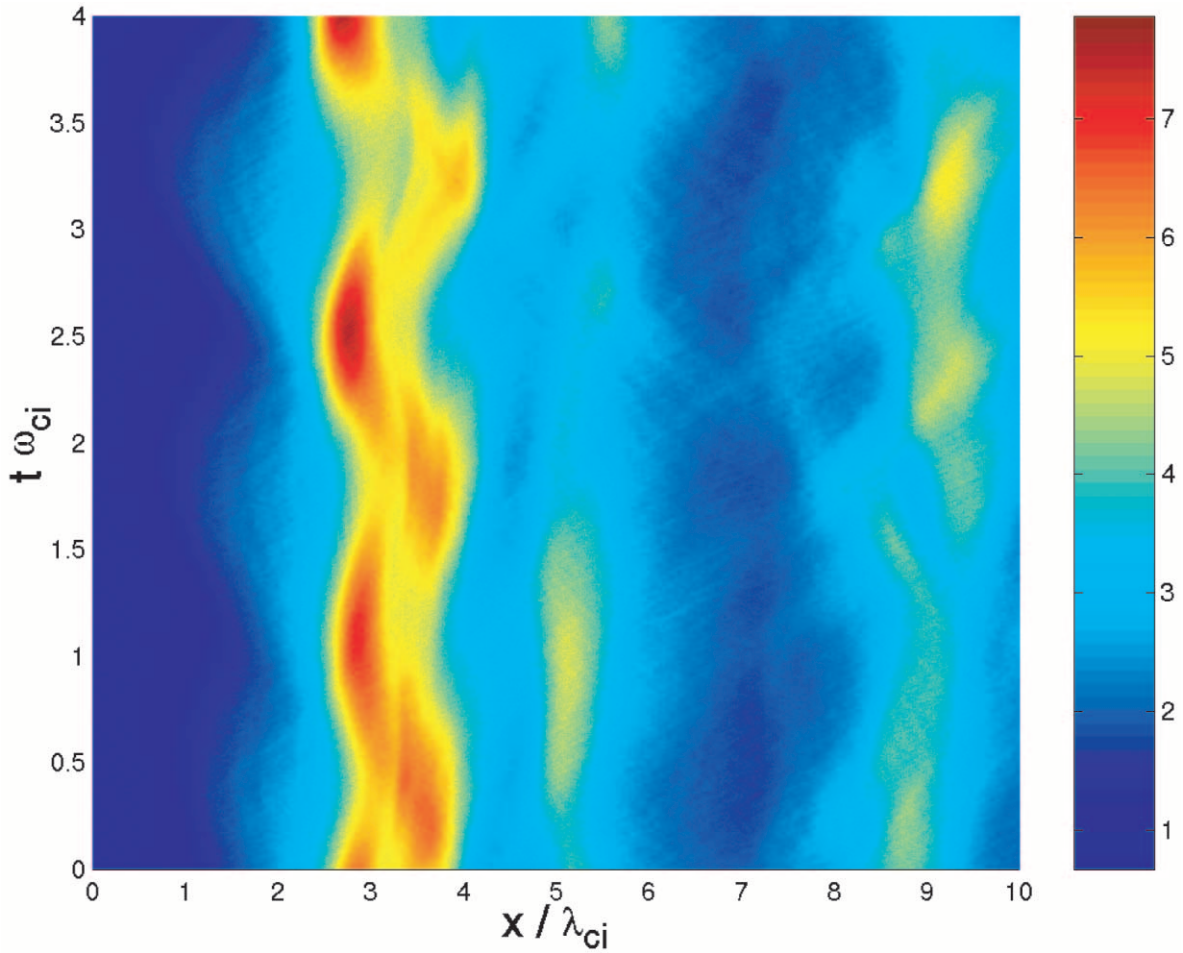

FIG. 5.—Perpendicular magnetic field component B_z as a function of position and time for $\beta = 1$. The field is normalized to the upstream magnetic field. The frame of reference is the shock rest frame.

modes with a downstream-directed phase velocity appear in the perpendicular magnetic field. These waves also have a wavelength comparable to the electron Larmor radius, but their phase velocity and hence their frequency is much larger. The last maximum of this second wave mode seems to be initializing the next magnetic overshoot. With this, the foot almost dies down and a new cycle begins.

The $\beta = 1$ results (Fig. 5) also show a time-dependent behavior. The magnetic overshoot region oscillates in the x direction and the size of the foot region pulsates with the same time period, which is of the order of the ion cyclotron period. The waves inside the foot that could be seen clearly in the $\beta = 0.15$ case still exist, but are much weaker. Thus, they are not visible in the color plot of the magnetic field. A major difference to the low β case is the absence of any shock reformation events.

4. ANALYSIS

To quantify the differences in the foot of the shock for the two cases $\beta = 0.15$ and $\beta = 1$, we have taken a small region $x_{\min} < x < x_{\max}$ and $t_{\min} < t < t_{\max}$ that lies inside the foot region. The values of the bounding parameters are given in Table 2. The perpendicular magnetic field and the parallel electric field were sampled with 512×2048 grid points for $\beta = 0.15$ and 256×2048 grid points for $\beta = 1$ in the x and t directions. A two-dimensional Fourier transform was applied after Hanning windowing to compensate for the nonperiodicity of the data.

The low-β Fourier-transformed fields $\hat{B}_z(k, \omega)$ and $\hat{E}_x(k, \omega)$ show very clear structure, as shown in Figures 6 and 7. Three different modes can be observed in the perpendicular magnetic field. Two modes (at higher ω) show a hyperbolic shape in (ω, k) space crossing the ω axis at about 1.5–2 ω_{pe}. (Here the electron plasma frequency is calculated with the upstream undisturbed conditions.) Assuming a density rise of a factor 3 in the foot as compared to the upstream plasma, the local plasma frequency would be $\omega_{pe,f} = 3^{1/2}\, \omega_{pe} \approx 1.73\, \omega_{pe}$. One of these modes has a much higher amplitude than the other and opens into a much nar-

TABLE 2

TIME AND SPACE WINDOWS OF THE FOURIER TRANSFORMS

Bounding Parameters	$\beta = 0.15$	$\beta = 1$
$x_{\min}$	0.08	0.97
$x_{\max}$	3.92	2.21
$t_{\min}$	2.45	1.13
$t_{\max}$	2.90	2.28

NOTE.—Dimensions of the windows for which the Fourier transforms of electric and magnetic field have been calculated. Values for $\beta = 0.15$ and $\beta = 1$ correspond to coordinates in Figs. 4 and 5, respectively.

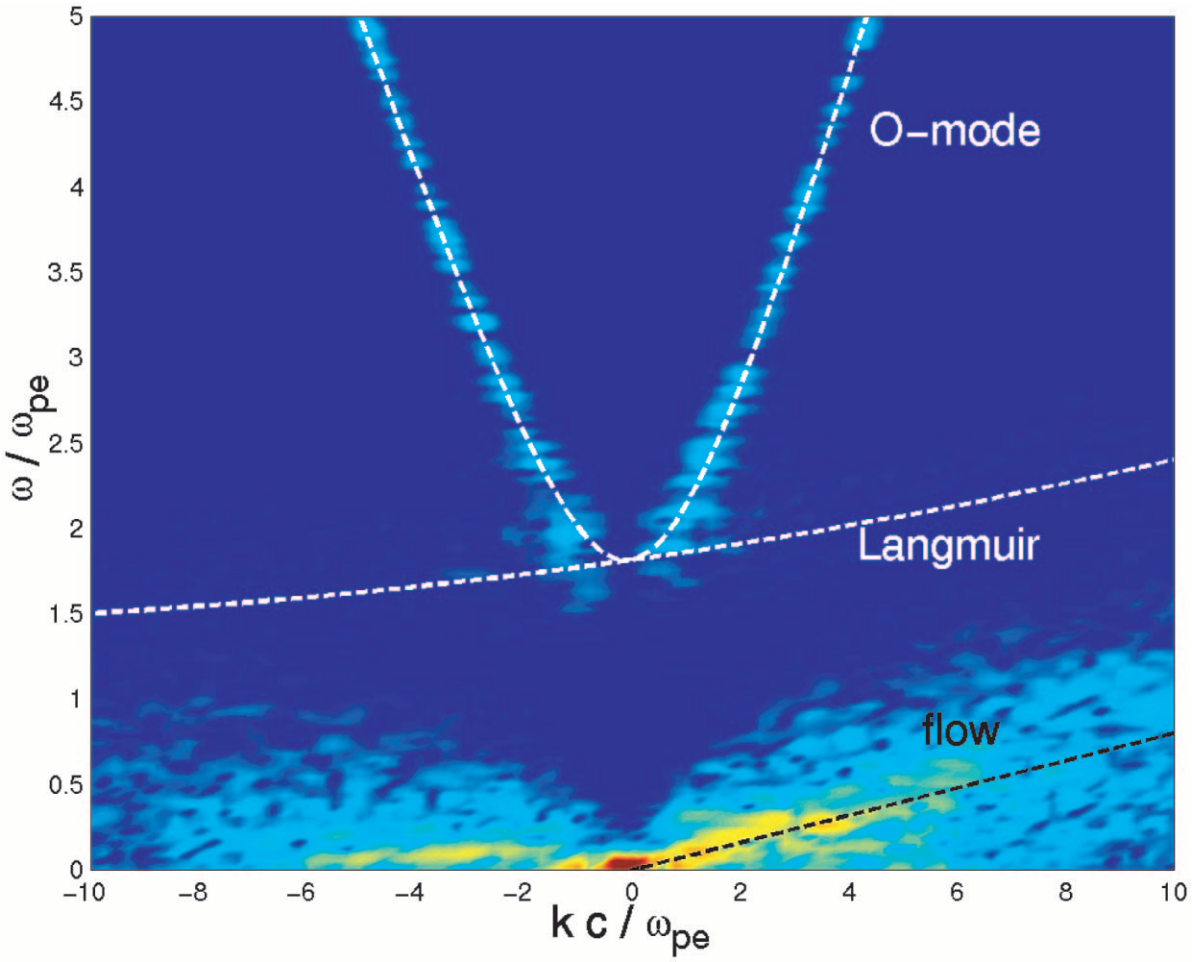

FIG. 6.—Fourier transform of the perpendicular magnetic field B_z in the foot of the shock for $\beta = 0.15$. The graphs for the dispersion relations for the Doppler-shifted O mode and Langmuir mode as well as the constant ion inflow velocity have been added.

rower hyperbola. This high-amplitude mode can be associated with the O mode

$$\frac{c^2k^2}{\omega^2} = 1 - \frac{\omega_{pe,f}^2}{\omega^2}\,, \tag{3}$$

or the X mode

$$\frac{c^2k^2}{\omega^2} = 1 - \frac{\omega_{pe,f}^2}{\omega^2}\frac{\omega^2 - \omega_{pe,f}^2}{\omega^2 - \omega_{pe,f}^2 - \omega_{ce}^2}\,. \tag{4}$$

Since $\omega_{ce}^2 \ll \omega_{pe,f}^2$, the two dispersion relations differ only slightly and cannot be distinguished on a graph with the resolution of Figure 6. However, the X mode would have contributions in both components of the electric field perpendicular to $\boldsymbol{B}$. Since we do not see this mode in the Fourier-transformed electric field $\hat{E}_x$, we infer that the mode excited is in fact the O mode. A closer look at the Fourier-transformed fields reveals a small asymmetry. This can easily be explained by a Doppler shift originating from the fact that the plasma in the foot is not at rest with respect to the shock. Adding a Doppler shift v_0 to the dispersion relation (eq. [3]), we obtain

$$\frac{c^2k^2}{(\omega - v_0k)^2} = 1 - \frac{\omega_{pe,f}^2}{(\omega - v_0k)^2}\,. \tag{5}$$

We find that a density rise of a factor 3.3 in the foot together with $v_0 = 0.08c$ produces good agreement, and we infer this velocity to be the velocity of the inflowing ion beam relative to the shock front, as discussed further below. The resulting dispersion relation is plotted in Figure 6.

The second mode intersecting the ω axis at $\omega_{pe,f}$ opens into a much wider hyperbola and has low magnetic field amplitude but larger electric field amplitude. This mode can be interpreted in terms of the suggestion by Papadopoulos (1988) that Langmuir waves should be present in the foot of the shock. The Doppler-shifted dispersion relation for Langmuir waves is

$$(\omega - v_0k)^2 = \omega_{pe,f}^2 + k^2v_{\mathrm{th},f}^2\,, \tag{6}$$

where $v_{\mathrm{th},f}$ is the thermal velocity of the electrons in the foot of the shock. Since electron heating is very effective in the low-β case, the thermal velocity of the electrons in the foot is enhanced compared to the undisturbed conditions. From an electron phase space distribution taken at a time between $t_{\min}$ and $t_{\max}$, we determine the factor $v_{\mathrm{th},f} \approx 6.4v_{\mathrm{th},1}$, with $v_{\mathrm{th},1}$ being the upstream thermal velocity. The dispersion relation (eq. [6]) taken with this thermal velocity is plotted in Figure 7. Here a value of $v_0 = 0.045c$ yields the best fit to the data. There remains some deviation from the dispersion relation for negative wavenumbers. This can be explained

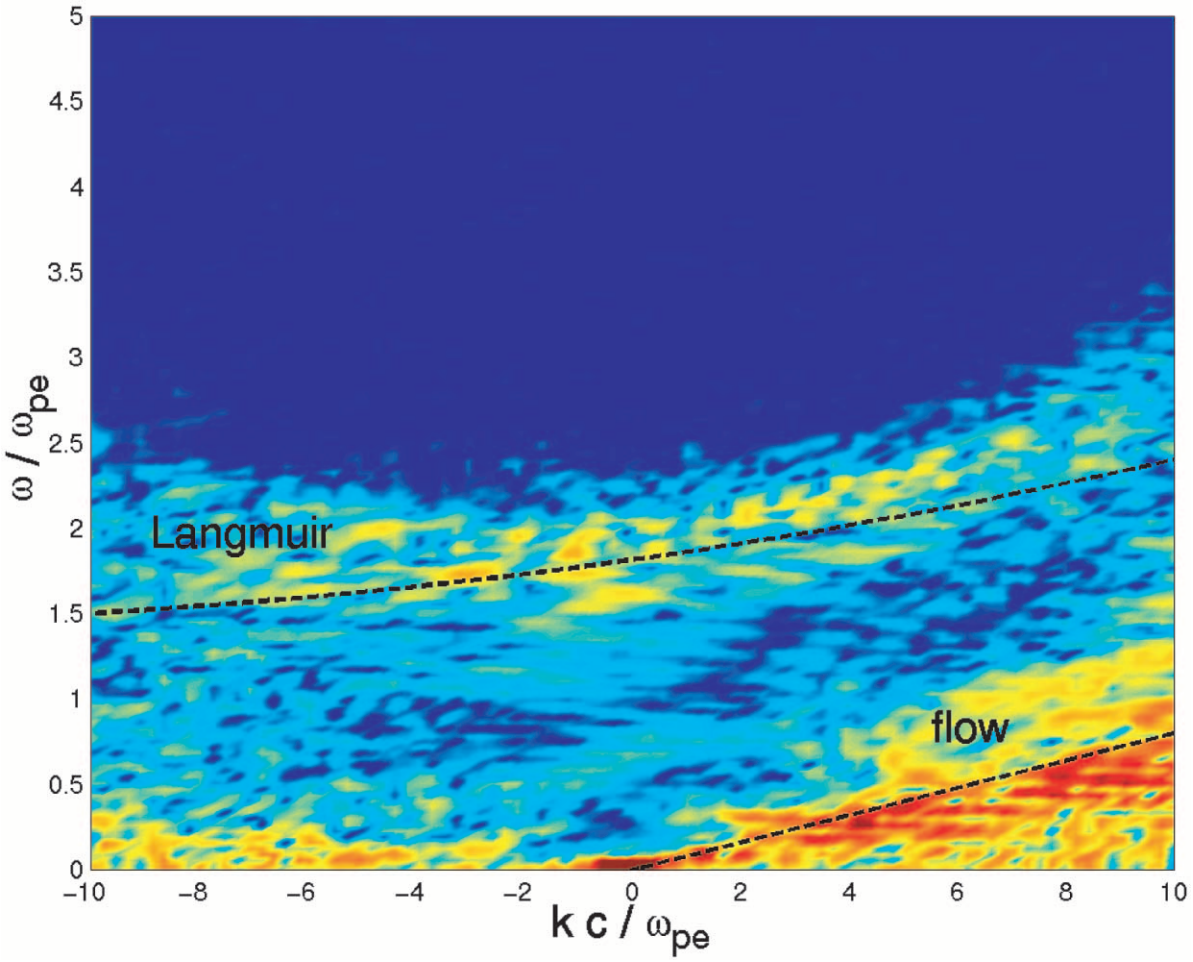

FIG. 7.—Fourier transform of the parallel electric field E_x in the foot of the shock for $\beta = 0.15$. The graphs for the dispersion relation for the Doppler-shifted Langmuir mode as well as the constant ion inflow velocity have been added.

by the fact that there is no unique flow velocity in the strongly varying foot region during the time window of the Fourier transform. The variance in flow velocities and thus the velocity of the Doppler shift creates some spread in the ω-k diagram. The weak signature of these electrostatic waves in the magnetic field can be understood by nonlinearities caused by the high intensity of these waves. The electric currents caused by the high amplitude wave create a magnetic field component which is neglected in the linear analysis but can become visible in the nonlinear regime. In contrast, the fact that these waves can be observed at all remains to be explained, since the spatially one-dimensional simulation only allows waves traveling perpendicular to $\boldsymbol{B}$ (recall that B_x was identically zero). The waves are unaffected by the magnetic field if the frequency ω of the wave is large compared to the electron cyclotron frequency $\omega \gg \omega_{ce,f}$. Since $\omega \geq \omega_{pe,f}$ and

$$\frac{\omega_{pe,f}}{\omega_{ce,f}} = \frac{1}{\sqrt{3}}\frac{\omega_{pe}}{\omega_{ce}} = \frac{20}{\sqrt{3}} \gg 1 \ , \qquad (7)$$

this condition is always fulfilled.

Another clearly visible mode that can be seen in both Figures 6 and 7 intersects the origin with a constant positive slope corresponding to a velocity of about $0.08c$, which coincides with the velocity of the inflowing ion beam. This mode in the ω-k diagram can thus be identified with low-frequency modes traveling with the inflowing ions. The resolution of low-frequency modes is determined by the length of the time window over which the Fourier analysis has been carried out. The maximum time for this is given by the period of the oscillation of the foot, so that the low-frequency modes cannot be resolved.

The electric field parallel to the flow (Fig. 7) exhibits broadband noise whose maximum coincides with the positive phase velocity mode that is observed in the perpendicular magnetic field. Moreover, a clear cutoff with a hyperbolic shape that coincides with the weaker hyperbolic mode observed in $\hat{B}_z$ can be seen.

The Fourier transforms of B_z and E_x for the case of $\beta = 1$ show the same modes, however at a much lower level than for the low-β case. For the $\beta = 1$ case, the left-hand side of equation (1) evaluates to about 11, while the low-β case gives 73.5, so that the foot is susceptible to Buneman instabilities in both cases. However, the results indicate that the growth rate is much lower in the high-β case, so that waves cannot build up during the time taken by an electron to cross the foot region. This large difference in the growth rate has a major consequence. The slowly growing waves in the high-β case always stay in the linear regime. The fast-grow-

ing waves in the low-β case quickly leave the linear regime and form nonlinear structures. These can be observed as electron phase space holes coupled to ion solitons (Saeki & Rasmussen 1991).

Finally, we have determined the energy distribution of the electrons in the far downstream region. To this end, we have calculated the absolute magnitude of the velocity of every electron in the rightmost ion Larmor radius of the simulation and distributed the data into 1000 velocity bins. To improve the statistics, we have repeated this for every time step over one ion cyclotron period and integrated the results. The resulting energy distributions $f(E_{\rm kin})$, where $E_{\rm kin}$ is the kinetic energy of an electron for $\beta = 0.15$ and $\beta = 1$, are shown in Figure 8. The energy is normalized to the inflow kinetic energy of the electrons. Due to a small difference in the shock jump conditions for the different β, the inflow kinetic energy is slightly different for the two cases. The values for $mu^2_{\rm flow}/2$ are 1.47 keV for $\beta = 0.15$ and 1.44 keV for $\beta = 1$; hence, the difference is only about 2%. In addition, $\int_0^\infty f(E_{\rm kin})\, dE_{\rm kin} = 1$.

The two energy distributions shown in Figure 8 demonstrate that the value of β has great influence on the thermalization and acceleration of electrons in the shock. The distribution in the high-β case is almost thermal, with temperature calculated by regression to be $T_e = 3.08\ mu^2_{\rm flow}/2$, which is also plotted in Figure 8. In contrast, the energy distribution for the low-β case can be described by two temperatures. Up to about 20 times the upstream flow energy, the distribution follows a thermal distribution with $T_e = 2.90\ mu^2_{\rm flow}/2$. Above 30 times the upstream flow energy, the distribution shows a high-energy tail with a temperature of $T_e = 5.75\ mu^2_{\rm flow}/2$. This suggests that the increased level of wave activity in the foot of the shock for the low-β case is very efficient in accelerating the electrons. In the simulation with $\beta = 0.15$, electrons were accelerated to energies of up to 65 $mu^2_{\rm flow}$, which corresponds to about 95 keV.

5. CONCLUSIONS

We have simulated the high Mach number magnetosonic shock of a supernova remnant for two different values of the ratio β of kinetic pressure to magnetic pressure (where $\beta = \beta_i = \beta_e$ is the same for ions and electrons). The low-β case recovers the results of Shimada & Hoshino (2000), while the results of the high-β simulation show some distinct differences. However, the phase space distributions for $\beta = 0.15$ exhibit small-scale structures and holes in the electron phase space inside the foot; these features are absent for $\beta = 1$. In addition, the plot of the perpendicular magnetic field $B_z(x, t)$ for low β shows small-scale structures inside the foot, together with shock reformation processes. The time-dependent behavior is highly irregular. For high β, the perpendicular magnetic field $B_z(x, t)$ still shows time-dependent behavior, but the structure is more regular and periodic, and the small-scale structures are missing. Fourier analysis of $B_z(x, t)$ and $E_x(x, t)$ for $\beta = 0.15$ inside the foot of the shock displays a number of modes. The clearest can be identified as an O mode which is Doppler shifted with respect to the velocity of the inflowing ion population.

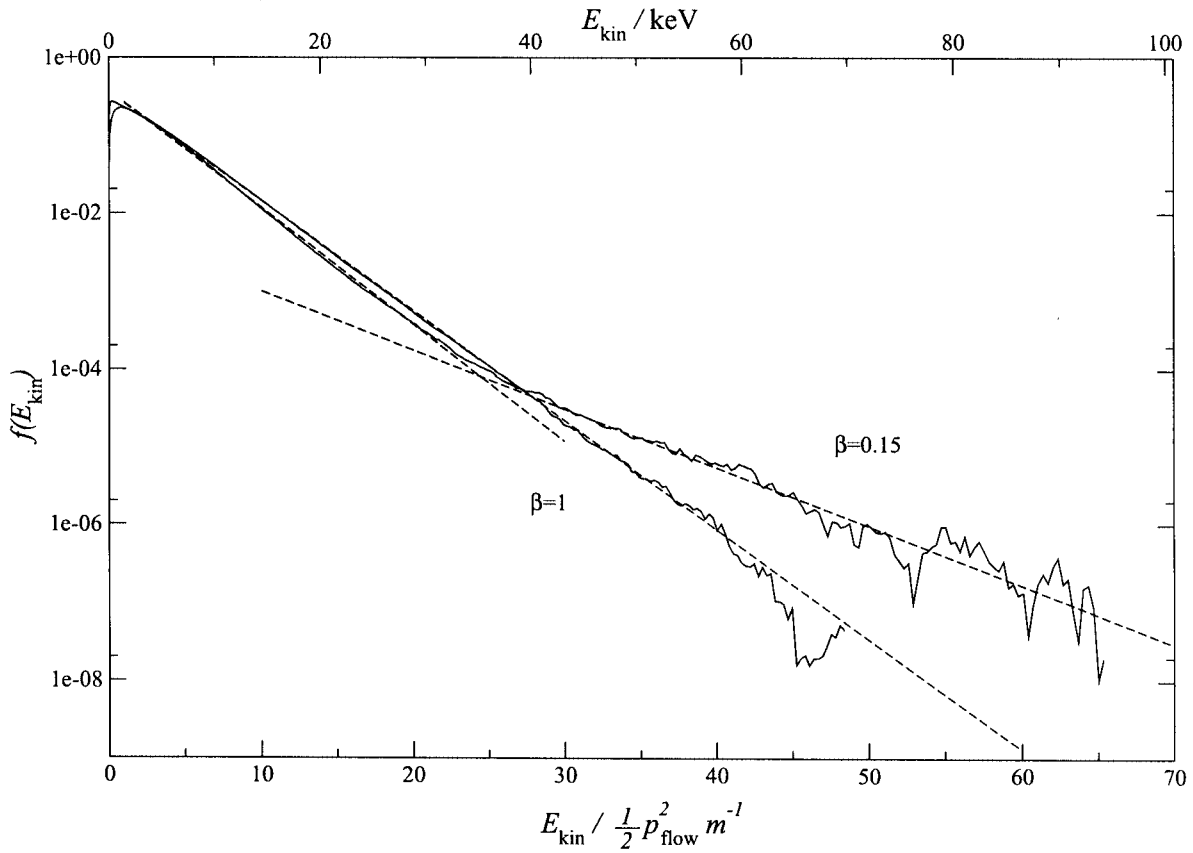

FIG. 8.—Energy distribution $f(E_{\rm kin})$ of electrons for $\beta = 0.15$ and $\beta = 1$ averaged over the rightmost ion Larmor radius of the simulation box and over one ion cyclotron period. The top axis shows the energy in keV, while the bottom axis is normalized to the inflow energy.

Fourier analysis for $\beta = 1$ shows the same modes, however with a much smaller amplitude. This means that an increase in the magnetic field or a decrease in the temperature of the undisturbed plasma will enhance instabilities in the foot of the shock. The resulting downstream electron distribution shows that the low-β shock produces a nonthermal energy distribution and is much more efficient at accelerating electrons to mildly relativistic energies. For $\beta = 0.15$, electrons with energies of up to 95 keV are observed.

Our results confirm that the plasma physics considered here and by Shimada & Hoshino (2000) may indeed contribute to the cosmic-ray electron injection at SNRs, and we have elucidated the underlying mechanisms in some detail. We have also found that relatively small changes in a key macroscopic dimensionless parameter of the system (the plasma β) can significantly alter the plasma microphysics. This affects the extent of electron acceleration, which is strongest at low β. Observationally, this places a constraint on the ratio of kinetic energy to magnetic field in astrophysical situations where this injection mechanism can operate. While it works well at lower β, other mechanisms should be sought if electron cosmic-ray injection is believed to occur in higher β (≥ 1) environments.

This work was supported in part by the Commission of the European Communities under TMR Astroplasmaphysics Network Contract ERB-CHRXCT980168. S. C. C. acknowledges a PPARC Lecturer Fellowship and R. O. D. support from the UK DTI. We are grateful to K. G. McClements for helpful comments.

APPENDIX A

THE SHOCK-FOLLOWING ALGORITHM

We developed a simple shock-following algorithm to be able to simulate the shock for longer times without increasing the size of the simulation box. For this we define the approximate position of the shock by the first position where the perpendicular magnetic field exceeds 3 times the upstream magnetic field,

$$x_s = \min[x : B_z(x) \geq 3\ B_{z,1}]\ . \tag{A1}$$

When the shock position thus defined approaches the left boundary of the system to within 4 Larmor radii λ_{ci}, we shift the whole system by one grid cell to the right. The particles in the rightmost cell are removed from the system, while the leftmost cell is filled up with additional particles whose distribution is that prescribed for newly injected particles. The right boundary of the simulation box is again taken to be completely reflecting. The fields at the left boundary are set according to the conditions of the undisturbed plasma, while everywhere else the fields are shifted to the right, including at the right boundary,

$$\boldsymbol{A}_{n+1}^{t+\Delta t} = \boldsymbol{A}_n^t \quad n = 0 \ldots N-1\ , \tag{A2}$$

where $\boldsymbol{A}_n^t$ stands for the electric and magnetic fields $\boldsymbol{E}$ and $\boldsymbol{B}$ at the grid point n and at time t; N is the number of grid points. The new boundary condition is redefined in terms of the new fields at this position,

$$\boldsymbol{E}_{\text{right}}^{\text{new}} = \boldsymbol{E}_N^{t++\Delta t} = \boldsymbol{E}_{N-1}^t\ . \tag{A3}$$

The whole procedure corresponds physically to the idea of inserting a new, perfectly reflecting and infinitely conducting boundary one grid position to the left of the former boundary. All the charges and currents of the grid cell that is dropped from the system are effectively accumulated on this right boundary. This ensures that, on the average, charges and currents cannot accumulate in the simulation box. Thus, after the system has evolved for some time, the shock will on average be at rest in the simulation box. However, all physical quantities in the simulation will be given in the downstream rest frame. The shock will then be about 25 λ_{ci} away from the right boundary (where λ_{ci} represents the Larmor radius of the highest energy particles in the system). This has been found from test simulations to be sufficiently far away to consider the shock well separated from the piston. By " sufficiently far," we mean that the shock has reached its quasi–steady, fully evolved state. The subsequent evolution of the shock is then independent of the distance back to the reflecting boundary, provided that this distance remains large, and we are then free to move the reflecting boundary forward in small increments.

REFERENCES

Bell, A. R. 1978, MNRAS, 182, 147
Bennett, L., & Ellison, D. C. 1995, J. Geophys. Res., 100, 3439
Bessho, N., & Ohsawa, Y. 1999, Phys. Plasmas, 6, 3076
Buneman, O. 1958, Phys. Rev. Lett., 1, 8
Burgess, D., Wilkinson, W. P., & Schwartz, S. J. 1989, J. Geophys. Res., 94, 8783
Cargill, P. J. 1991, Adv. Space Res., 11, 241
Cargill, P. J., & Papadopoulos, K. 1988, ApJ, 329, L29
Chapman, S. C., & Cowley, S. W. H. 1984, J. Geophys. Res., 89, 7357
Cowley, S. W. H. 1977, Planet. Space Sci., 26, 539
Devine, P. 1995, Ph. D. thesis, Univ. Sussex
Dieckmann, M. E., McClements, K. G., Chapman, S. C., Dendy, R. O., & Drury, L. O. 2000, A&A., 356, 377
Ellison, D. C., & Reynolds, S. P. 1991, ApJ, 382, 242
Giacalone, J., Burgess, D., Schwartz, S., & Ellison, D. 1993, ApJ, 402, 550
Giacalone, J., & Jokipii, J. R. 1994, ApJ, 430, L137
Hockney, R. W., & Eastwood, J. W. 1981, Computer Simulations Using Particles (New York: McGraw Hill)
Jokipii, J. R. 1987, ApJ, 313, 842
———. 1993, Geophys. Res. Lett., 20, 1759
Jones, F. C., Jokipii, J. R., & Baring, M. G. 1998, ApJ, 509, 238
Koyama, K., Petre, R., & Gotthelf, E. V. 1995, Nature, 378, 255
Levinson, A. 1997, Mon. Notes Astron. Soc. South Africa, 278, 1018
McClements, K. G., Bingham, R., Su, J. J., Dawson, J. M., & Spicer, D. S. 1993, ApJ, 409, 465
Northrup, T. G., & Teller, E. 1960, Phys. Rev., 117, 215
Papadopoulos, K. 1988, Ap&SS, 144, 535
Pohl, M., & Esposito, J. A. 1998, ApJ, 507, 327
Quest, K. B. 1986, J. Geophys. Res., 91, 8805
Saeki, K., & Rasmussen, J. J. 1991, J. Phys. Soc. Japan, 60, 735
Shimada, N., & Hoshino, M. 2000, ApJ, 543, L67